fluids

MDPI

Article

Impact of Navier's Slip and MHD on a Hybrid Nanofluid Flow over a Porous Stretching/Shrinking Sheet with Heat Transfer

Thippaiah Maranna [1], Gadhigeppa Myacher Sachin [1], Ulavathi Shettar Mahabaleshwar [1], Laura M. Pérez [2] and Igor V. Shevchuk [3,*]

[1] Department of Studies in Mathematics, Shivagangotri, Davangere University, Davangere 577 007, India; marannat4@gmail.com (T.M.); u.s.m@davangereuniversity.ac.in (U.S.M.)
[2] Departamento de Ingeniería Industrial y de Sistemas, Universidad de Tarapaca, Casilla 7D, Arica 1000000, Chile; lperez@academicos.uta.cl
[3] Faculty of Computer Science and Engineering Science, TH Koln-University of Applied Sciences, 51643 Gummersbach, Germany
* Correspondence: igor_v.shevchuk@th-koeln.de

Abstract: The main objective of this study is to explore the inventive conception of the magneto-hydrodynamic flow of a hybrid nanofluid over-porous stretching/shrinking sheet with the effect of radiation and mass suction/injection. The hybrid nanofluid advances both the manufactured nanofluid of the current region and the base fluid. For the current investigation, hybrid nanofluids comprising two different kinds of nanoparticles, aluminium oxide and ferrofluid, contained in water as a base fluid, are considered. A collection of highly nonlinear partial differential equations is used to model the whole physical problem. These equations are then transformed into highly nonlinear ordinary differential equations using an appropriate similarity technique. The transformed differential equations are nonlinear, and thus it is difficult to analytically solve considering temperature increases. Then, the outcome is described in incomplete gamma function form. The considered physical parameters namely, magnetic field, Inverse Darcy number, velocity slip, suction/injection, temperature jump effects on velocity, temperature, skin friction and Nusselt number profiles are reviewed using plots. The results reveal that magnetic field, and Inverse Darcy number values increase as the momentum boundary layer decreases. Moreover, higher values of heat sources and thermal radiation enhance the thermal boundary layer. The present problem has various applications in manufacturing and technological devices such as cooling systems, condensers, microelectronics, digital cooling, car radiators, nuclear power stations, nano-drag shipments, automobile production, and tumour treatments.

Keywords: MHD; mass suction/injection; Prandtl number; radiation; Hnf; velocity slip

check for updates

Citation: Maranna, T.; Sachin, G.M.; Mahabaleshwar, U.S.; Pérez, L.M.; Shevchuk, I.V. Impact of Navier's Slip and MHD on a Hybrid Nanofluid Flow over a Porous Stretching/Shrinking Sheet with Heat Transfer. *Fluids* **2024**, *9*, 180. https://doi.org/10.3390/fluids9080180

Academic Editor: Sergey Smolentsev

Received: 25 June 2024
Revised: 3 August 2024
Accepted: 7 August 2024
Published: 10 August 2024

Copyright: © 2024 by the authors. Licensee MDPI, Basel, Switzerland. This article is an open access article distributed under the terms and conditions of the Creative Commons Attribution (CC BY) license (https://creativecommons.org/licenses/by/4.0/).

1. Introduction

The potential uses of nanotechnology in a variety of industries have recently attracted the attention of many researchers. In terms of their thermophysical characteristics, base fluids are distinct from nanofluids, which have confined heat conductivity. The suspended nanoparticles have a diameter that is typically smaller than one nanometer. Ordinary liquids like water and ethylene have low thermal conductivities, which restricts their ability to be used individually in a variety of practical sectors. Choi et al. [1] first invented nanofluids in 1995 as a solution for improving thermal performance. Choi found that nanoparticles have more heat conductivity than base fluid. Nanoliquids have numerous uses in the fields of automobiles, electronics, nuclear reactors, and cancer therapies. Crane et al. [2] may have originally looked at the flow across a linearly stretched surface.

Lately, substantial research has been conducted on a novel class of nanofluids; these fluids are referred to as hybrid nanofluids. Hybrid nanofluids have better thermal characteristics as a result of the combined effect of their several components. Because of their

several advantages over nanoparticles, which were discovered in recent research through the insertion of different nanoparticles in the operating fluid, they have gained widespread attention from researchers. Presently, many studies are attempting to create hybrid nanofluids or blends of nanofluids, which integrate two different sorts of nanoparticle. In their analysis of heat transmission, Hayat et al. [3] considered a hybrid nanofluid formed by a mixture of CuO-Ag. Sun et al. [4] conducted an experimental study to estimate how the rate of transmission of heat for the (Fe_3O_4/H_2O) nanoparticles varied within circular horizontal pipes subjected to magnetic field effects. Sun discovered a direct correlation between the amplitude of magnetic field and speed of heat exchange. A hybrid nanofluid composed of water and platinum/graphene nanoplatelets was studied by Yarmand et al. [5] in a four-sided microchannel whose borders were preserved by steady heat flux. Waini et al. [6] explored constant motion and transferred heat through a penetrable stretching/shrinking sheet in an Hnf and convective barrier constraints.

Magnetohydrodynamics is a discipline of fluid dynamics that deals with electrically conductive fluids. This field of study developed in the late 1950s and early 1960s, with an emphasis on re-entry surface heating in spaceships. Mahabaleshwar et al. [7] investigated steady magnetohydrodynamics, an incompressible Hnf flow, and the movement of mass induced by penetrable strengthening sheets with quadratic speed. Sneha et al. [8] studied the flow of an Hnf and water through an elongating or contracting sheet in an inclined MHD Casson fluid accompanied by a mixed convective BL flow. Zainal et al. [9] revealed an MHD Hnf Al_2O_3-Cu/water flow through a penetrable stretching/shrinking sheet under the influence of quadratic speed. Devi et al. [10] studied a Cu-Al_2O_3/water flow with a hydromagnetic influence in the direction of stretching sheet, and they identified that Hnf has a faster speed of heat transmission compared to a regular fluid, which is Cu/water. Tripathi et al. [11] focused on mathematical and numerical treatments of magnetohemodynamics over a damaged artery with (Ag-Au/blood) redundant stenosis in the presence of an outward radially magnetic field. Recently, according to Asghar et al. [12], the Tiwari-Das model was used to describe a 3D Hnf movement via a rotating extending/contraction surface in a magnetic field as well as during joule heating.

Thermal radiation, which influences heat transmission, is used in a wide range of technological operations, such as operating gas turbines and nuclear power plants, as well as diverse propulsion systems used in aircraft, missiles, satellites, and spacecraft. However, the efficient Prandtl number is the only dimensionless quantity employed in the linearized Rosseland approximation, and linear radiation is invalid for large temperature differences. Mahabaleshwar et al. [13] reported a precise mathematical solution for an Hnf flow across a stretching/shrinking sheet in the presence of radiation and mass transpiration. Reddy et al. [14] perceives the modelling of an Hnf flow through a stretching/shrinking sheet for a chemical reaction, suction, slip impact, and radiation, adopting unstable magnetohydrodynamic heat and mass transfer. Tulu et al. [15] studied the mixed convection flow of a hybrid nanofluid (MWCNTs-Al_2O_3/engine oil) over a spinning cone in the presence of thermal radiation and variable viscosity. Rosca et al. [16] presented a BL flow and heat transfer properties through a porous isothermal stretching/shrinking sheet employing both Nf and Hnf flows. Bakar et al. [17] explored the characteristics of flow and exchanges in mixed convection in the presence of an Hnf in a penetrable media with a heat source, suction/injection, radiation, and MHD. Gul et al. [18] investigated the flow of a nanofluid with MWCNTs and SWCNTs dispersed in ethane-1,2-dio used in a Darcy–Forchheimer porous material beyond an extending cylinder with numerous slips. Moreover, the researchers described hybrid nano-fluid models with several effects on flows, which can be observed in [17–23].

From the above analysis, we have plenty of motivation to begin this study after several scientists researched numerous analytical fluids and distinct nanoparticles, leading to the development of significant thermal properties. However, as far the authors know, there has been no analytical study of a 2D hybrid nanoparticle flow past a permeable stretching/shrinking sheet, while considering the MHD, radiation, suction/injection, and slip

condition. In order to fill this gap, the novelty of the present research is an investigation of the magnetohydrodynamic flow of an *Hnf* past a permeable stretching/shrinking sheet considering the effect of radiation and mass suction/injection. Aluminium oxide (Al_2O_3) and a ferrofluid (Fe_3O_4) are dissolved in water to create the studied hybrid nanofluid. The PDEs were turned into a collection of ODEs using similarity transformations. To determine analytical solutions for the simplified ODEs, the impacts of different control parameters—magnetic field, inverse Darcy number, radiation, velocity slip condition, temperature, skin friction, and Nusselt number—are graphically illustrated. This contemporary investigation can be utilized in various fields, such as solar collectors, permafrost melting, hot extrusion, heat engines, heat exchangers, thermocouples, etc. More specifically, the following points contribute to the uniqueness of the problem.

(i) Small magnetic particles colloidally suspended in a liquid medium are called ferrofluid. Ferrofluid have some significant applications in heat exchangers and can be used for mechanical dampening in loudspeakers.
(ii) Nanoparticles of metallic oxides, such as Al_2O_3, SiO_2, ZnO, and TiO_2, can easily be dissolved in base liquids, and Al_2O_3 is one of these metal oxides with high thermal properties.
(iii) The Darcy phenomenon is taken into account by the fluid flow.
(iv) The Lorentz force tends to accelerate body forces, which increase flow velocity and develop a thicker momentum boundary layer.

2. Materials and Methods

Let us assume a steady 2D laminar flow of an electrically conducting MHD Hnf through a uniformly porous stretching/shrinking sheet intersecting with region $y = 0$, the flow is restrained to $y > 0$. The flow is moving towards the x-axis and the y-axis is orthogonal to it. The applied B_0 is determined along the normal sheet. It is also presumed that the constant wall and maximum temperature of the fluids are T_w and T_∞. Moreover, it should be noted that water is a basic fluid containing two different nanoparticles, aluminium oxide (Al_2O_3) and ferrofluid (Fe_3O_4) (as shown in Figure 1).

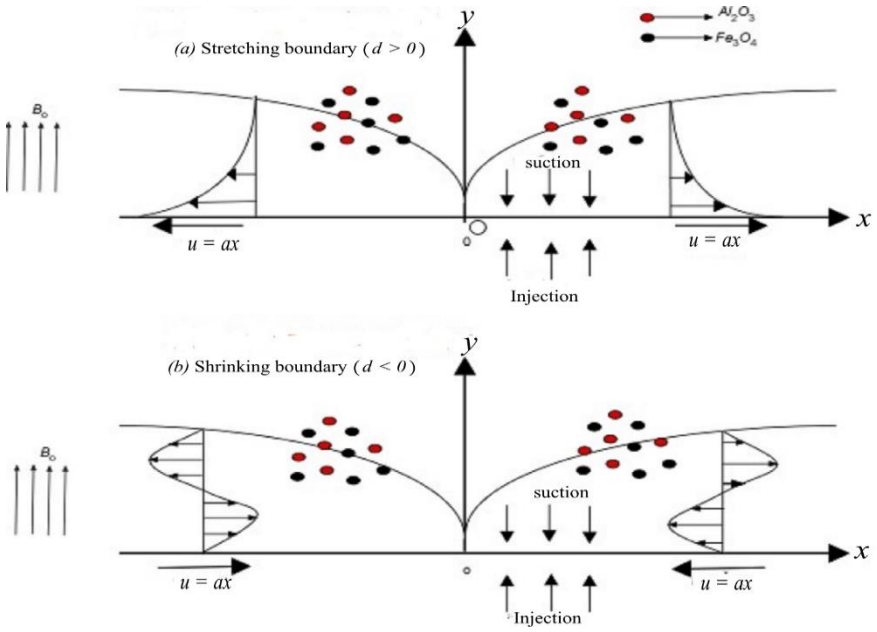


Figure 1. Diagrammatic representation of fluid flow.

Under the above assumptions, the dimensional governing equation for this problem [24–26] can be stated as follows.

Continuity equation:

$$\frac{\partial u}{\partial x} + \frac{\partial v}{\partial y} = 0, \tag{1}$$

Momentum equation:

$$u\frac{\partial u}{\partial x} + v\frac{\partial u}{\partial y} = \nu_{hnf}\frac{\partial^2 u}{\partial y^2} - \frac{\sigma_{hnf}B_0^2}{\rho_{hnf}}u - \frac{\nu_{hnf}}{K_a}u, \tag{2}$$

Energy equation:

$$u\frac{\partial T}{\partial x} + v\frac{\partial T}{\partial y} = \frac{\kappa_{hnf}}{(\rho C_p)_{hnf}} - \frac{1}{(\rho C_p)_{hnf}}\frac{\partial q_r}{\partial y}, \tag{3}$$

Here, the boundary conditions associated with the problem [27] are as follows:

$$\left.\begin{array}{ll} u(x,y) = dax + l_1\frac{\partial u}{\partial y}, \quad v(x,y) = s_1, \quad \theta(x,y) = 1 + k_1\frac{\partial T}{\partial y}, & \text{at } y = 0 \\ u(x,y) = 0, \quad \theta(x,y) = 0, & \text{at } y = \infty \end{array}\right\}, \tag{4}$$

where (u, v) symbolizes the velocity component along the (x, y) axes, respectively. The kinematic viscosity of the Hnf is indicated by symbol ν_{hnf}, density is represented by ρ_{hnf}, κ_{hnf} is the thermal conductivity, with heat capacitances indicated by the symbol $(\rho C_p)_{hnf}$. Here, $d > 0$ represents the stretching sheet, and $d < 0$ represents the shrinking sheet, respectively. s is the wall suction/injection parameter, while $s > 0$ is suction, and $s < 0$ is injection. The descriptions of the other parameters are mentioned in the nomenclature section.

Similarity Transformations

The previous equation is true as a certain outcome of using a similarity transformation, which supports obtaining the following solution [28]:

$$\left.\begin{array}{lll} u = axf'(\eta), & v = -\sqrt{a\nu_f}f(\eta), & \eta = \sqrt{\frac{a}{\nu_f}}y \\ \theta(\eta) = \frac{T - T_\infty}{T_w - T_\infty} & & \end{array}\right\}, \tag{5}$$

Here, prime denotes the differentiation by η, and ν_f is the dynamic viscosity of the fluid.

Furthermore, the radiant heat flux q_r is calculated by utilizing the Rosseland approximations for radiation [29–32]:

$$q_r = -\frac{4\sigma^*}{3k^*}\frac{\partial T^4}{\partial y}, \tag{6}$$

where σ^* and k^* signify the Stefan–Boltzman constant and coefficient of mean absorption, correspondingly. Presume that temperature fluctuations inside the motion are sufficiently small, such that T^4. The equation can be written as linear functions of temperature, T, by implementing Taylor series expansion and omitting higher order terms; thus, T^4 is reduced to

$$T^4 \cong 4T_\infty^3 T - 4T_\infty^4, \tag{7}$$

after differentiating terms using Equation (6), we obtain:

$$\frac{\partial q_r}{\partial y} = -\frac{16\sigma^*}{3k^*}\frac{\partial^2 T}{\partial y^2}, \tag{8}$$

Now, Equation (3) becomes

$$u\frac{\partial T}{\partial x} + v\frac{\partial T}{\partial y} = \left(\frac{\kappa_{hnf}}{(\rho C_p)_{hnf}} + \frac{16\sigma^* T_\infty^3}{3k^*(\rho C_p)_{hnf}}\right)\frac{\partial^2 T}{\partial y^2}. \tag{9}$$

Equation (1) is automatically fulfilled, and Equations (2) and (3) are transformed to highly nonlinear ODEs by employing similarity variables (5):

$$\frac{d^3f}{d\eta^3} + A\left\{f(\eta)\frac{d^2f}{d\eta^2} - \left(\frac{df}{d\eta}\right)^2\right\} - A_3A_1\frac{\sigma_f B_0^2}{\rho_f a}\frac{df}{d\eta} - Da^{-1}\frac{df}{d\eta} = 0, \tag{10}$$

$$(A_4 + N_r)\frac{d^2\theta}{d\eta^2} + \mathrm{Pr}A_5 f(\eta)\frac{d\theta}{d\eta} = 0, \tag{11}$$

with transformed boundary conditions, which are as follows:

$$\left.\begin{array}{l}\left(\frac{df}{d\eta}\right)_{\eta=0} = d + l_1\left(\frac{d^2f}{d\eta^2}\right)_{\eta=0}, \quad f(\eta)_{\eta=0} = s_1, \quad \theta(\eta) = 1 + k_1\left(\frac{d\theta}{d\eta}\right)_{\eta=0} \\ \left(\frac{df}{d\eta}\right)_{\eta=\infty} = 0, \quad \theta(\eta)_{\eta=\infty} = 0\end{array}\right\}. \tag{12}$$

where

$$\begin{aligned} A_1 &= \tfrac{\mu_{hnf}}{\mu_f} = \tfrac{1}{(1-\varphi_1)(1-\varphi_2)}, \\ A_2 &= \tfrac{\rho_{hnf}}{\rho_f} = (1-\varphi_2)\left[(1-\varphi_1)\rho_f + \varphi_1\rho_{s1}\right] + \varphi_2\rho_{s2}, \\ A_3 &= \tfrac{\sigma_{hnf}}{\sigma_f}, \quad A_4 = \tfrac{\kappa_{hnf}}{\kappa_f}, \text{ and } A_5 = \tfrac{(\rho C_p)_{hnf}}{(\rho C_p)_f}. \end{aligned}$$

and

$Da^{-1} = \frac{\mu_f}{\rho_f K_a}$ is the inverse Darcy number,

$\mathrm{Pr} = \frac{\mu_f (C_p)_f}{k_f}$ is the Prandtl number,

$N_r = \frac{16\sigma^* T_\infty^3}{3k^*\kappa_f}$ is the radiation parameter,

Now, we recommended a similarity conversion as follows:

$$f(\eta) = \frac{1}{\sqrt{A}}F(\chi), \quad \theta(\eta) = \phi(\chi), \quad \chi = \sqrt{A}\eta. \tag{13}$$

After employing Equation (13) in Equations (10) and (11), we obtain the following formula:

$$\frac{d^3F}{d\chi^3} + \left\{F(\chi)\frac{d^2F}{d\chi^2} - \left(\frac{dF}{d\chi}\right)^2\right\} - A_3M\frac{dF}{d\chi} - \frac{Da^{-1}}{A}\frac{dF}{d\chi} = 0, \tag{14}$$

$$\frac{d^2\phi}{d\chi^2} + \frac{\mathrm{Pr}A_5}{(A_4 + N_r)A}F(\chi)\frac{d\phi}{d\chi} = 0, \tag{15}$$

with boundary conditions as follows:

$$\left.\begin{array}{l}\left(\frac{dF}{d\chi}\right)_{\chi=0} = d + L\left(\frac{d^2F}{d\chi^2}\right)_{\chi=0}, \quad F(\chi)_{\chi=0} = s, \quad \phi(\chi) = 1 + K^*\left(\frac{d\phi}{d\chi}\right)_{\chi=0} \\ \left(\frac{dF}{d\chi}\right)_{\chi\to\infty} = 0, \quad \phi(\chi)_{\chi\to\infty} = 0\end{array}\right\}. \tag{16}$$

where

$A = A_1A_2$, $M = \frac{1}{A_2}\frac{\sigma_f B_0^2}{\rho_f a}$ is the magnetic field, $s = \sqrt{A}s_1$, $L = \sqrt{A}l_1$, $K^* = \sqrt{A}k_1$.

For physical quantities of interest, the following information is sufficient:

$$\left(\frac{d^2f}{d\eta^2}\right)_{\eta=0} = \sqrt{A}\left(\frac{d^2F}{d\chi^2}\right)_{\chi=0}, \quad -\left(\frac{d\theta}{d\eta}\right)_{\eta=0} = -\sqrt{A}\left(\frac{d\phi}{d\chi}\right)_{\chi=0}. \tag{17}$$

Hence, having estimated $\left(\frac{d^2F}{d\chi^2}\right)_{\chi=0}$ and $\left(\frac{d\phi}{d\chi}\right)_{\chi=0}$ from (16), for any specific operating fluid with skin friction $\left(\frac{d^2f}{d\eta^2}\right)_{\eta=0}$ and the heat transfer $\left(\frac{d\theta}{d\eta}\right)_{\eta=0}$, we can perhaps examine something clearly by multiplying $\left(\frac{d^2F}{d\chi^2}\right)_{\chi=0}$ and $\left(\frac{d\phi}{d\chi}\right)_{\chi=0}$ via consistent $\sqrt{A}$ from (17).

3. Analytical Solution for Momentum

In this section, we assume that the analytical solution for Equation (14) satisfying Equation (16) is defined [27] as follows:

$$F(\chi) = s + d\frac{1 - e^{-\lambda\chi}}{\lambda(1 + L\lambda)}, \tag{18}$$

According to (18), the velocity profile is as follows:

$$\frac{dF}{d\chi} = \frac{d}{1 + L\lambda}e^{-\lambda\chi}. \tag{19}$$

The boundary conditions in Equation (16) are directly satisfied by this solution with $\lambda > 0$, indicating that a physical flow exists. Equation (18) can be substituted into Equation (14) to produce the following third-order algebraic expression:

$$L\lambda^3 + (1 - sL)\lambda^2 - \left(s + ML + \frac{Da^{-1}L}{A}\right)\lambda - \left(A_3M + d + \frac{Da^{-1}}{A}\right) = 0. \tag{20}$$

As a result, it is possible to only have one positive root for $\lambda > 0$ according to Descartes' rule of signs, when $d > 0$, because there can only be one modification in the sign of the factors. Despite the fact that Equation (20) may be simplified to a cubic polynomial, the exact manifestation of the positively useful actual root λ of Equation (20), which is necessary to determine momentum and skin friction, can be provided and Equation (20) can be rewritten in the following form:

$$\delta_1\lambda^3 + \delta_2\lambda^2 - \delta_3\lambda - \delta_4 = 0. \tag{21}$$

where

$\delta_1 = L$, $\delta_2 = (1 - sL)$, $\delta_3 = \left(s + ML + \frac{Da^{-1}L}{A}\right)$, and $\delta_4 = \left(A_3M + d + \frac{Da^{-1}}{A}\right)$. where the roots are as follows

$$\lambda_1 = -\frac{\delta_2}{3\delta_1} - \frac{2^{\frac{1}{3}}\left(-\delta_2^2 - 3\delta_1\delta_3\right)}{3\delta_1 p^{\frac{1}{3}}} + \frac{p^{\frac{1}{3}}}{3 * 2^{\frac{1}{3}}\delta_1}, \tag{22a}$$

$$\lambda_{2,3} = -\frac{\delta_2}{3\delta_1} + \frac{\left(1 \pm i\sqrt{3}\right)\left(-\delta_2^2 - 3\delta_1\delta_3\right)}{3 * 2^{\frac{1}{3}}\delta_1 p^{\frac{1}{3}}} - \frac{\left(1 \mp i\sqrt{3}\right)p^{\frac{1}{3}}}{6 * 2^{\frac{1}{3}}\delta_1}. \tag{22b}$$

Here,

$$p = -2\delta_2^3 - 9\delta_1\delta_2\delta_3 + 27\delta_1^2\delta_4 + \sqrt{4\left(-\delta_2^2 - 2\delta_1\delta_3\right)^3 + \left(-2\delta_2^3 - 9\delta_1\delta_2\delta_3 + 27\delta_1^2\delta_4\right)^2}$$

Although Equation (22a) has a unique solution, in Equation (22b), another solution exists for $d = -1$. It must be highlighted that Equation (22a), which includes the parameter p, corresponds to complex branches. Thus, although complex numbers are required for a formal cubic solution, when added together, the imaginary components cancel each other -out. It is possible to completely re-express the real root in relation to actual quantities, but this may necessitate additional computation.

4. Heat Transfer Solution

Now, when we substitute Equation (18) into Equation (15), we obtain the following:

$$\frac{d^2\phi}{d\chi^2} + \frac{\mathrm{Pr}A_5}{(A_4+N_r)A}\left\{s + d\frac{(1-e^{-\lambda\chi})}{\lambda(1+L\lambda)}\right\}\frac{d\phi}{d\chi} = 0, \tag{23}$$

In order to solve the above equation, which employs a variable transformation approach, a novel approach to the issue conceivably explored. A new variable $t = -e^{-\lambda\chi}$ is initiated and substituted into Equation (23), once we attain

$$t\frac{d^2\phi}{dt^2} + (\xi_1 - \xi_2 t)\frac{d\phi}{dt} = 0, \tag{24}$$

where

$\xi_1 = 1 - \frac{\mathrm{Pr}A_5 s}{\lambda A(A_4+N_r)} - \frac{\mathrm{Pr}A_5 d}{\lambda A^2(1+L\lambda)(A_4+N_r)}$, and $\xi_2 = \frac{\mathrm{Pr}A_5 d}{\lambda^2(1+L\lambda)A(A_4+N_r)}$. together with boundary conditions

$$\phi(\chi)_{\chi=-1} = 1 + K^*\lambda\left(\frac{d\phi}{d\chi}\right)_{\chi=-1}, \quad \phi(\chi)_{\chi=0} = 0. \tag{25}$$

Now, differentiate Equation (24) twice, and we can obtain the following form:

$$\phi(t) = \frac{c_1}{\xi_2^{1-\xi_1}}\int_0^{\xi_2 t} \sigma^{1-\xi_1-1}e^{\sigma}d\sigma + c_2, \tag{26}$$

Also, it can be written as follows:

$$\phi(t) = \frac{c_1}{\xi_2^{1-\xi_1}}\Gamma(1-\xi_1,\ \xi_2 t) + c_2, \tag{27}$$

Here,

$\sigma = \xi_2 t$, and $\Gamma(1-\xi_1, t) = \int_0^{\xi_2 t} t^{1-\xi_1}e^t dt$.

By applying the boundary conditions to the aforementioned Equation (27),

$$\phi(\chi)_{\chi=-1} = 1 + K^*\lambda\left(\frac{d\phi}{d\chi}\right)_{\chi=-1}, \quad \phi(\chi)_{\chi=0} = 0.$$

We will obtain the values of constants as follows:

$$\begin{aligned} c_1 &= -\frac{\xi_2^{1-\xi_1}}{K^*\lambda e^{-\xi_2} + [\Gamma(1-\xi_1,0) - \Gamma(1-\xi_1,\xi_2)}, \\ c_2 &= \frac{\Gamma(1-\xi_1,0)}{K^*\lambda e^{-\xi_2} + [\Gamma(1-\xi_1,0) - \Gamma(1-\xi_1,\xi_2)}. \end{aligned} \tag{28}$$

Equation (27) becomes

$$\phi(t) = \frac{e^{-\xi_2}\{\Gamma(1-\xi_1,0) - \Gamma(1-\xi_1,\xi_2 t)\}}{K^*\lambda\xi_2^{1-\xi_1} + e^{\xi_2}\{\Gamma(1-\xi_1,0) - \Gamma(1-\xi_1,\xi_2)\}}. \tag{29}$$

This exact solution clearly fulfils the boundary requirements and is simple to verify via a direct substitution into Equation (15), which calculates the exact solution we in terms of incomplete gamma function for energy expression. By substituting t into (29), we directly obtained the energy profile in terms of χ.

The Nusselt number gradient is then accomplished through Equation (29) as follows:

$$Nu = \left(\frac{d\theta}{d\eta}\right)_{\eta=0} = -\sqrt{A}\lambda \frac{\xi_2^{1-\xi_1}}{K^*\lambda\xi_2^{1-\xi_1} + e^{\xi_2}\Gamma(1-\xi_1,0) - e^{\xi_2}\Gamma(1-\xi_1,\xi_2)}. \quad (30)$$

According to Equation (30), the local heat transfer rate will approach zero at the significant temperature slip K^* limit. Ultimately, the benefits and efficiency of the current strategy are more clearly explained in detail in the following section.

5. Results

The current analytical problem considers the steady laminar flow of an MHD Hnfs flow in the attendance of mass suction/injection, as well as radiation. An influence of velocity slip and temperature slip is also studied in the current problem. Analytical solutions are provided for the flow governing Equations (14) and (15), together with boundary conditions (16). Table 1 outlines the thermophysical characteristics of the base fluid (water) as well as *Hnf*. For the numerical computation, the relevant thermophysical characteristics of nanoparticles and numerical values are obtained from Table 2. It was found that the comparison of present results is in a good agreement with those reported by Turkyilmazoglu et al. [28], as shown in Table 3. The nanoparticle volume fraction was reported to be in the range of $0 < \varphi < 0.02$. The value of Pr is set at 6.2. We adopt constant values to control parameter throughout the computation as follows: $0 < M < 100$, $0.6 < Da^{-1} < 5$, $0.05 < L < 100$, and $0.5 < s < 4$, $0.01 < K^* < 0.4$, $0.1 < N_r < 0.5$. This section displays pictorial results on velocity, temperature, $f_{\eta\eta}(0)$ and $-\theta_\eta(0)$ profiles for several values of magnetic field, inverse Darcy number, velocity slip, mass suction/injection, radiation and temperature jump parameters are studied.

Table 1. Thermophysical characteristics of Hnfs [7–11,13].

Characteristics	**Hnfs**
Density	$\rho_{hnf} = (1-\varphi_2)\left[(1-\varphi_1)\rho_f + \rho_{s1}\right] + \varphi_2\rho_{s2}$
Heat capacity	$(\rho C_p)_{hnf} =$ $(1-\varphi_1)\left[(1-\varphi_1)(\rho C_p)_f + \varphi_1(\rho C_p)_{s1}\right] +$ $\varphi_2(\rho C_p)_{s2}$
Dynamic viscosity	$\mu_{hnf} = \frac{\mu_f}{(1-\varphi_1)^{2.5}(1-\varphi_2)^{2.5}}$
Thermalconductivity	$\kappa_{hnf} = \frac{\kappa_f(\kappa_{s2}+2\kappa_{bf}+2\varphi_2(\kappa_{s2}-\kappa_f))}{(\kappa_{s2}+2\kappa_{bf}-(\kappa_{s2}-\kappa_f))}$ where $\kappa_{bf} = \frac{\kappa_f(\kappa_{s1}+\kappa_f+2\varphi_1(\kappa_{s1}-\kappa_f))}{(\kappa_{s1}+2\kappa_f-(\kappa_{s1}-\kappa_f))}$
Electricalconductivity	$\sigma_{hnf} = \frac{\sigma_{s2}+2\sigma_{nf}-2\varphi_2(\sigma_{nf}-\sigma_{s2})}{\sigma_{s2}+2\sigma_{nf}+2\varphi_2(\sigma_{nf}-\sigma_{s2})} * \sigma_f$ where $\sigma_{nf} = \frac{\sigma_{s1}+2\sigma_f-2\varphi_1(\sigma_f-\sigma_{s1})}{\sigma_{s1}+2\sigma_f+\varphi_1(\sigma_f-\sigma_{s1})} * \sigma_f$

Where φ_1 and φ_2 are the solid volume capacity values of the aluminium oxide and ferrofluid, respectively.

The impact of velocity slip and magnetic field on the skin friction coefficient through a porous stretching/shrinking sheet of hybrid nanofluids Al_2O_3-Fe_3O_4/H_2O is depicted in Figures 2 and 3. Figure 2 displays the effect of velocity slip and the skin friction profile for a shrinking sheet case, while keeping other parameter values fixed at $M = 0.5$ and $Da^{-1} = 0.5$. The figure shows that the velocity slip parameter L rises in magnitude in both solution branches, which allows more fluid to slip over a surface, the $f_{\eta\eta}(0)$ profile diminishes in strength and becomes closer to zero for a larger quantity of L, i.e., the flow operates as though it were inviscid. Thus, it is assumed that there is no longer any friction

involving the sheet and the fluid and that the fluid no longer experiences any motion due to sheet stretching, leading to the flow appearance of inviscidity. Figure 3 reveals the variations of the skin friction profile in relation to M. It is clear from this figure that as the magnitude of M improves, the skin friction value decreases, all becoming asymptote for high s at the wall. This is proven by the existence of M, which decreases the thickness of the velocity and momentum BL and increases the velocity gradient at the wall.

Table 2. Numerical quantities of fluid and nanoparticles [33–35].

Nanoparticle/Base Fluid	$\rho\left(\mathbf{kg/m^3}\right)$	$\kappa\left(\mathbf{Wm^{-1}/K}\right)$	$C_p\left(\mathbf{Jkg^{-1}K^{-1}}\right)$	$\sigma(\mathbf{S/m})$
Water (H_2O)	997.1	0.613	4179	0.05
Aluminium oxide (Al_2O_3)	3970	765	40	1×10^{-10}
Ferrofluid (Fe_3O_4)	5180	9.7	650	0.74×10^{-10}

Table 3. Comparison of present study and related studies by other researchers.

Related Studies by Other Authors	Fluids	Value of λ
Turkyilmazoglu et al. [28]	Non-Newtonian	$F(\zeta) = s + d\frac{1-e^{-\lambda\chi}}{\lambda(1+L\lambda)}$ $L\lambda^3 + (1-sL)\lambda^2 -$ $(s+mL)\lambda - (m+d) = 0$
Present problem	Non-Newtonian	$F(\chi) = s + d\frac{1-e^{-\lambda\chi}}{\lambda(1+L\lambda)}$ $L\lambda^3 + (1-sL)\lambda^2 -$ $\left(s + ML + \frac{Da^{-1}L}{A}\right)\lambda -$ $\left(A_3M + d + \frac{Da^{-1}}{A}\right) = 0$

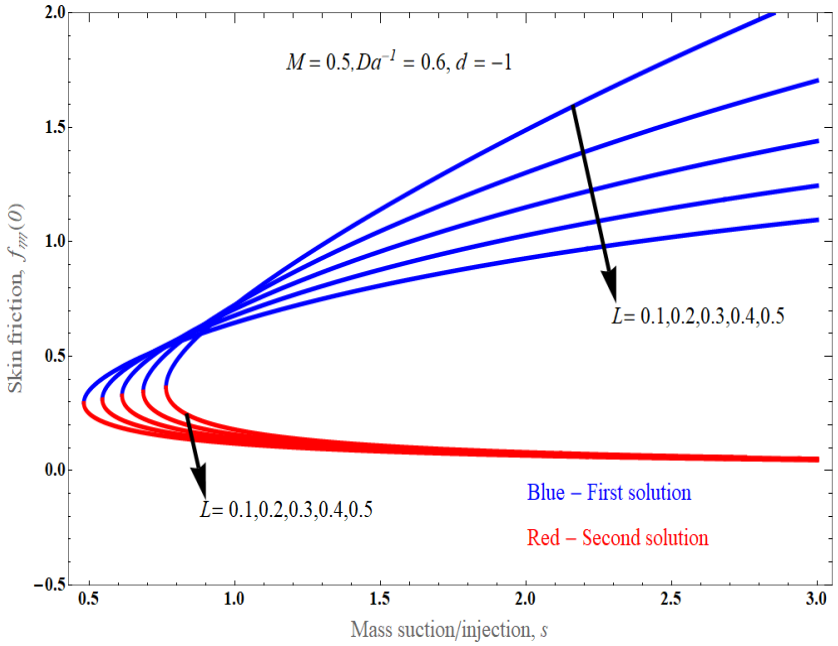


Figure 2. The impact of velocity slip parameter on skin friction.

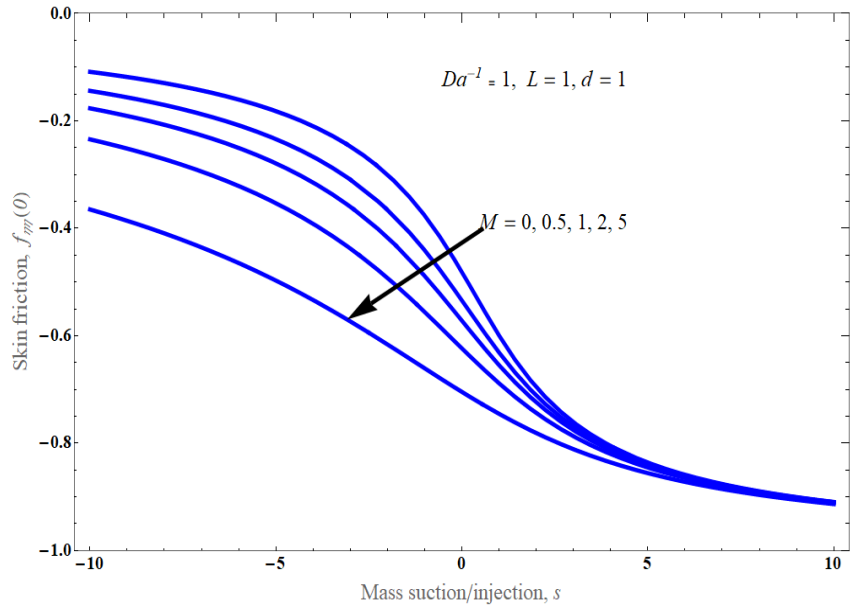


Figure 3. The impact of magnetic field on skin friction.

The role of the suction/injection parameter in the radial velocity $f(\eta)$, and axial velocity $\frac{df}{d\eta}$ for hybrid Al_2O_3-Fe_3O_4/H_2O nanofluids are shown in Figures 4 and 5 respectively, when $d = 1,\ 0.5 \leq M \leq 1,\ 0.5 \leq Da^{-1} \leq 1$, and $0.1 \leq L \leq 0.2$. Figure 4 shows that s increases with a significant increase in velocity. Whereas Figure 5 display the effect of s on momentum. From Figure 5 it is revealed that the nanofluid velocity decreases with increasing values of the mass suction/injection parameter, respectively. From Figure 5, we found that as the suction/injection parameter was elevated, the velocity declined.

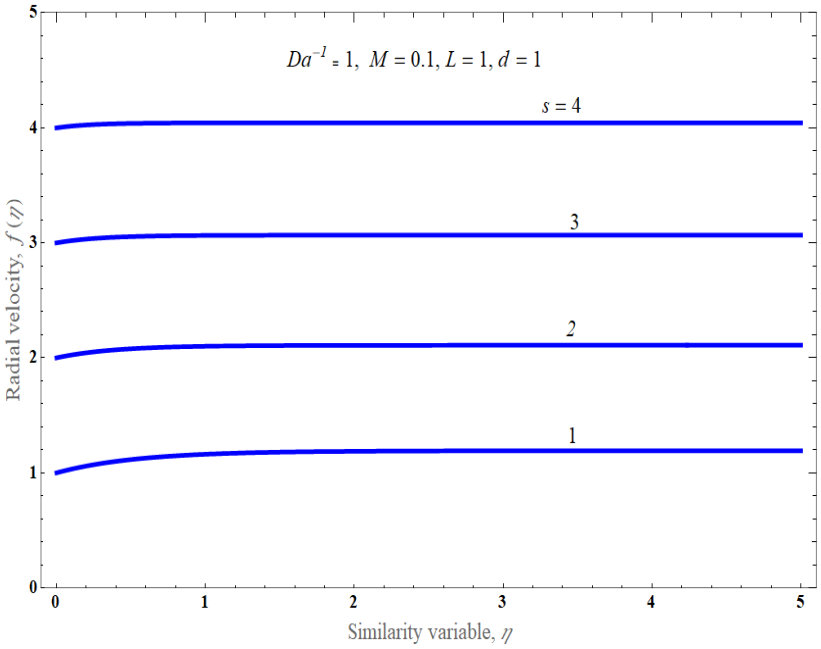


Figure 4. The impact of mass suction/injection on the radial velocity profile.

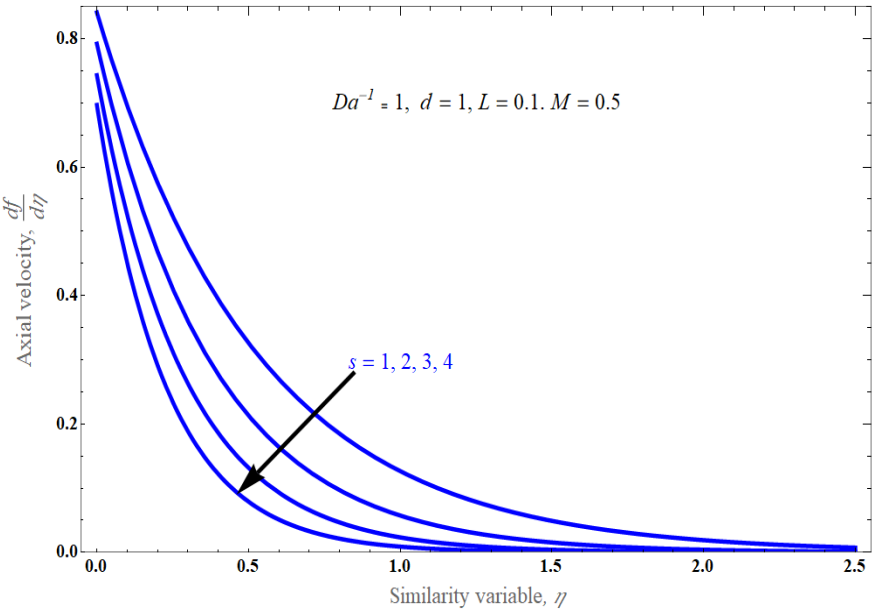


Figure 5. The impact of mass suction/injection on the velocity profile.

The non-dimensional velocity $\frac{df}{d\eta}$ for different quantities of M are observed in Figure 6. For several values of M, the momentum profile is exemplified in Figure 6. It is noted that as the magnitude of M increases, the flow velocity significantly reduces throughout the liquid domain. A drag-like force stated as the Lorentz force is generated when M is applied to an electrically conducting fluid. As a result, the fluid velocity within the BL decreases because the magnetic field prevents the transport phenomenon. Figure 7 characterizes profiles of the hybrid nanofluid velocity for various values of inverse Darcy number Da^{-1} with fixed other values at $M = s = 0.5$, $d = 1$, and $L = 0.05$. It was discovered that as Da^{-1} increases, the permeability of the penetrable media decreases, and a definite reduction in fluid activity is achieved.

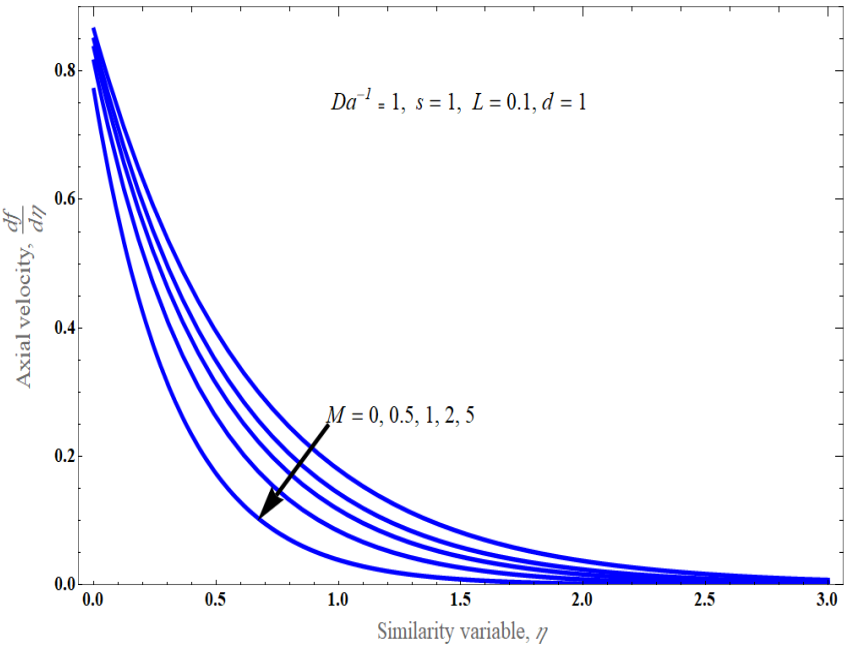


Figure 6. An impact of magnetic field on velocity profile.

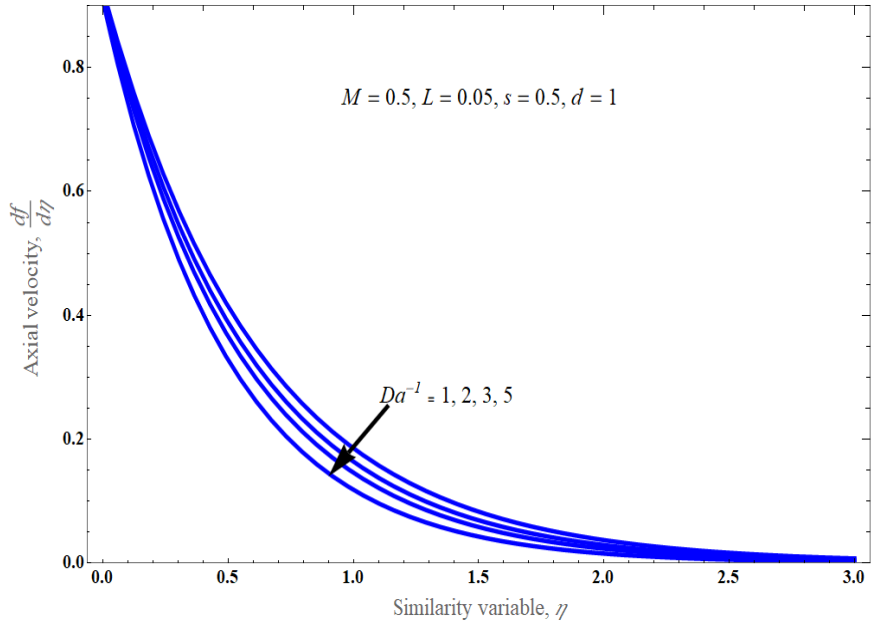


Figure 7. An impact of inverse Darcy number on velocity profile.

Figure 8 presents the effect of velocity slip L on the velocity profile. It is found that as the L values improve, the non-dimensional velocity profile declines. As the slip parameter increases, the fluid momentum reduces. When the slip condition increases, the stretching sheet velocity differs from the flow velocity close to the sheet. The effect of the suction/injection parameter on the temperature profiles as shown in the Figure 9. From Figure 9 it is revealed that the temperature decreases with increasing values of the mass suction/injection parameter, respectively. In case suction/injection, the fluid is moved nearer to the sheet under ambient conditions, which reduces the thickness of the thermal BL, as seen in Figure 9.

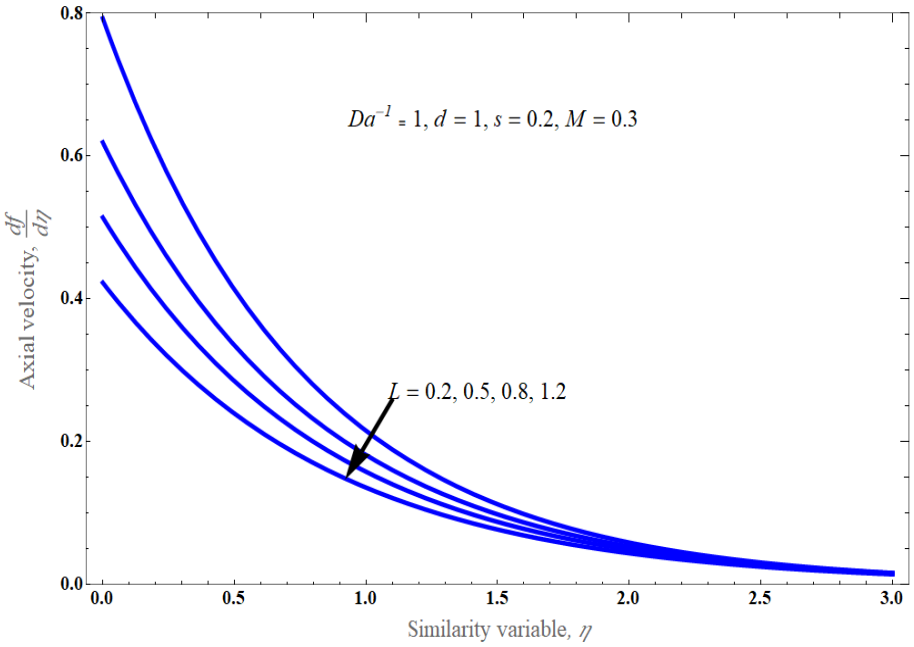


Figure 8. The impact of velocity slip on velocity profile.

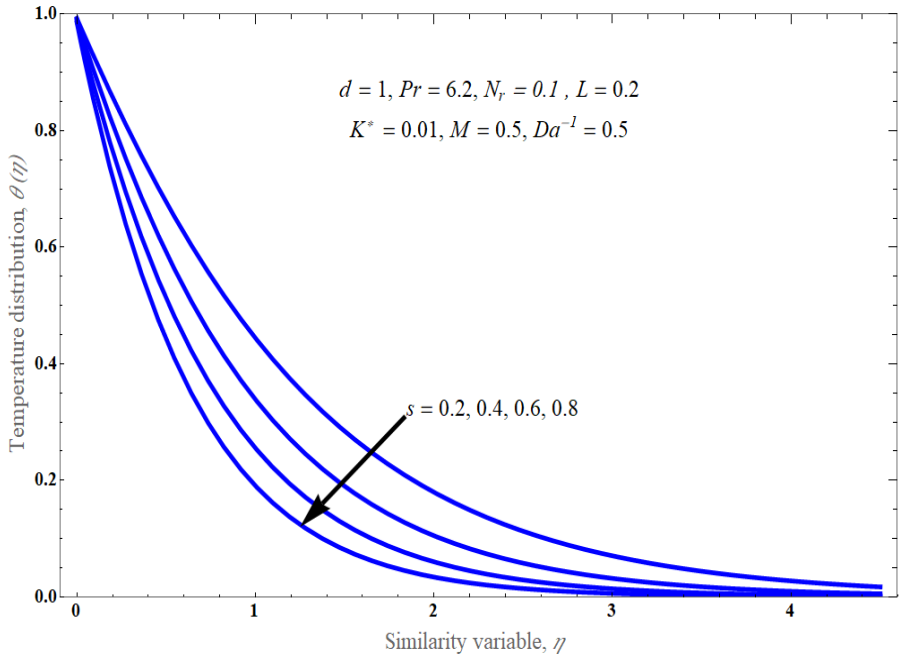


Figure 9. The impact of mass suction/injection on temperature distribution.

The key characteristics of magnetic field M on temperature profile as shown in the Figure 10. However, as shown in Figure 10, with rising magnetic values, the temperature profile rises. The flow experienced some friction as a result of the Lorentz force on velocity profiles; this friction ultimately boosted the flow temperature profile by causing the flow to produce more heat energy. Figure 11 exhibits the operation of Da^{-1} on temperature profile. Whenever the impact of the inverse Darcy number Da^{-1} increases, we noticed that the temperature of the fluid reduces. Additionally, we revealed that Da^{-1} has a significant impact on fluid thermal boundary layers.

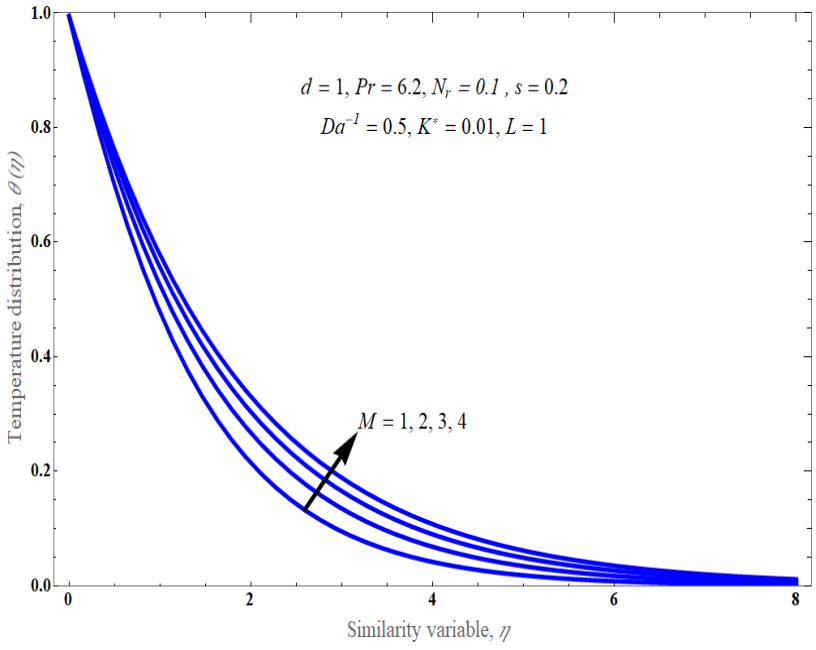


Figure 10. The impact of magnetic field on temperature distribution.

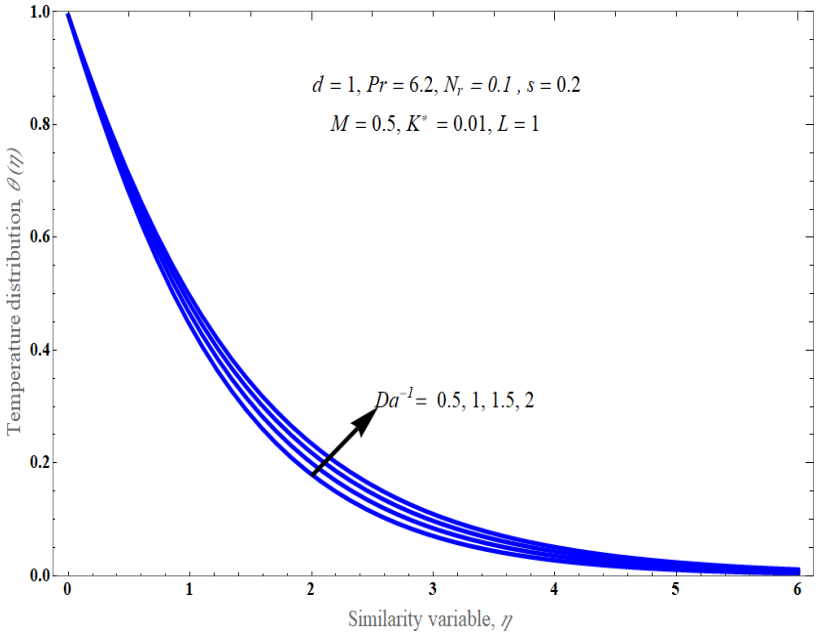


Figure 11. The impact of inverse Darcy number on temperature distribution.

Figure 12 demonstrates an impact of varying the velocity slip parameter L on the temperature distribution. When a temperature increase and magnetic field are present, it is found that temperature distribution increases as velocity slip parameter L value rises. Figure 13 shows the impact of temperature increase K^* on dimensionless temperature distribution. It is clearly demonstrated that by raising the strength of K^*, the temperature profile reduces. Although only a small amount of temperature transfer occurs between the sheet and the fluid, as the value of the temperature increase K^* grows, the thermal BL thickness depends.

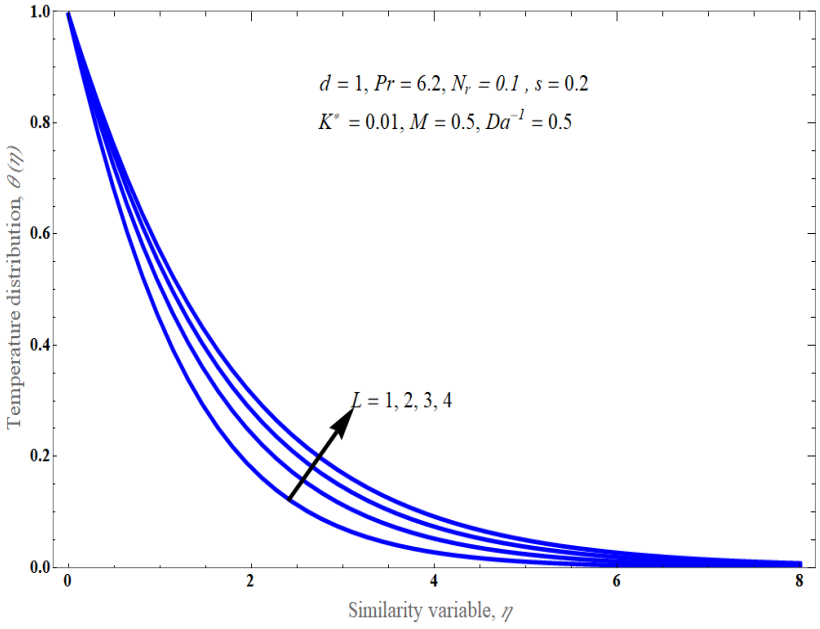


Figure 12. The impact of velocity slip parameter on temperature distribution.

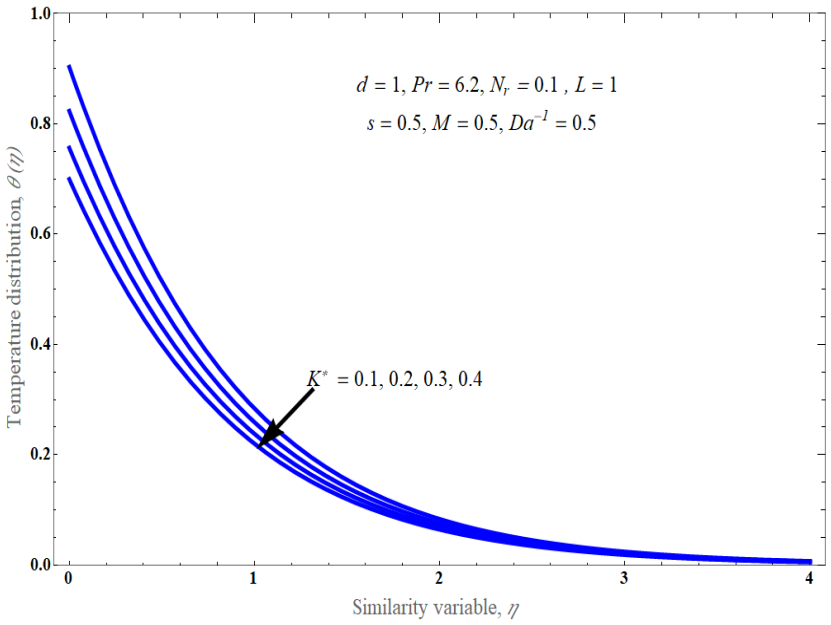


Figure 13. The impact of temperature increase on temperature distribution.

Figure 14 shows the effect of varying N_r parameters on temperature distribution. We found that radiation optimizes heat transmission because thermal BL rises as the thermal radiation increases. Significantly larger values of radiation increase the temperature of the operating fluid and thermal BL. According to Figures 15 and 16, the impacts of raising velocity slip L and M are identical, resulting in improved heat transfer. A substantial decrease in the speed of heat transmission is caused by a temperature increase.

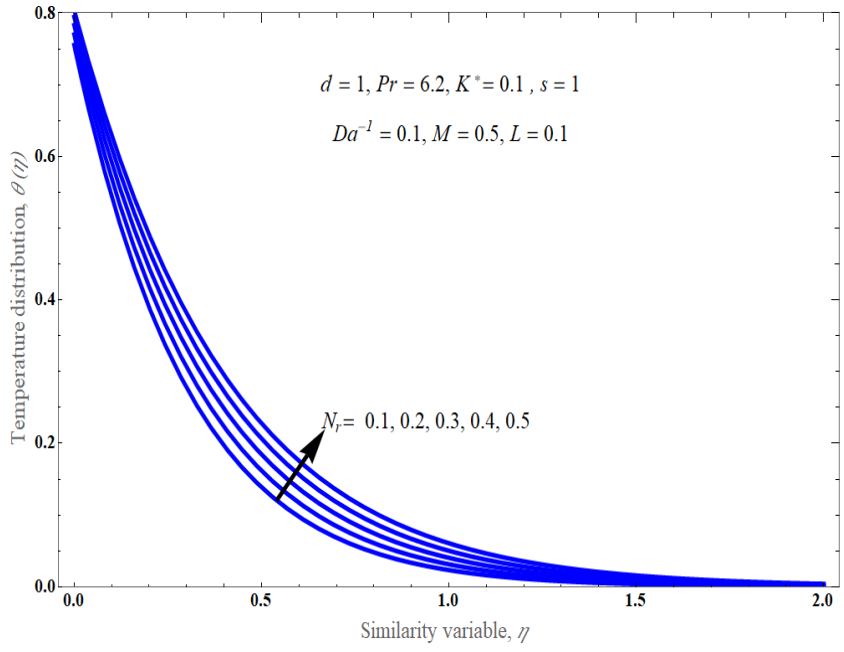


Figure 14. The impact of radiation on temperature distribution.

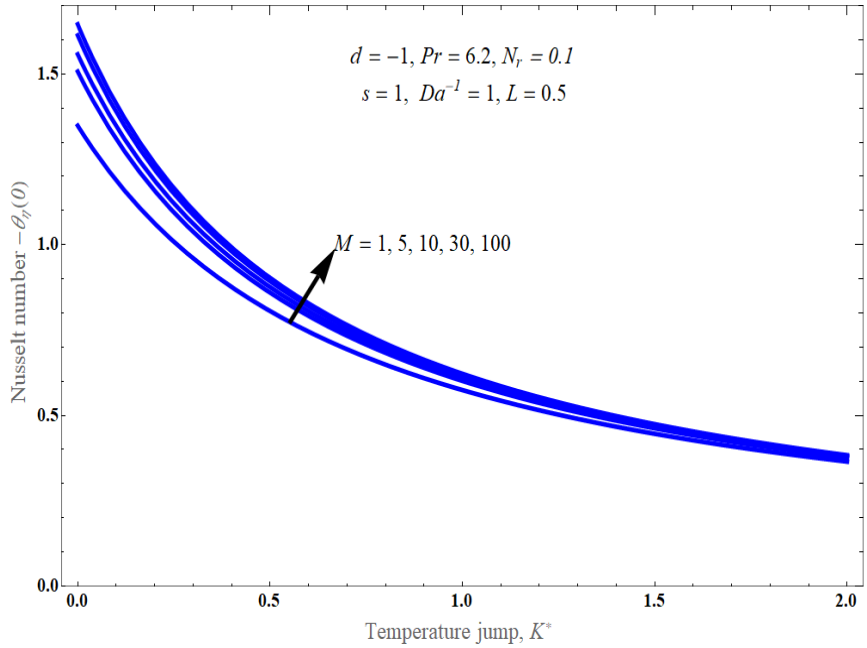


Figure 15. The impact of magnetic field on Nusselt number.

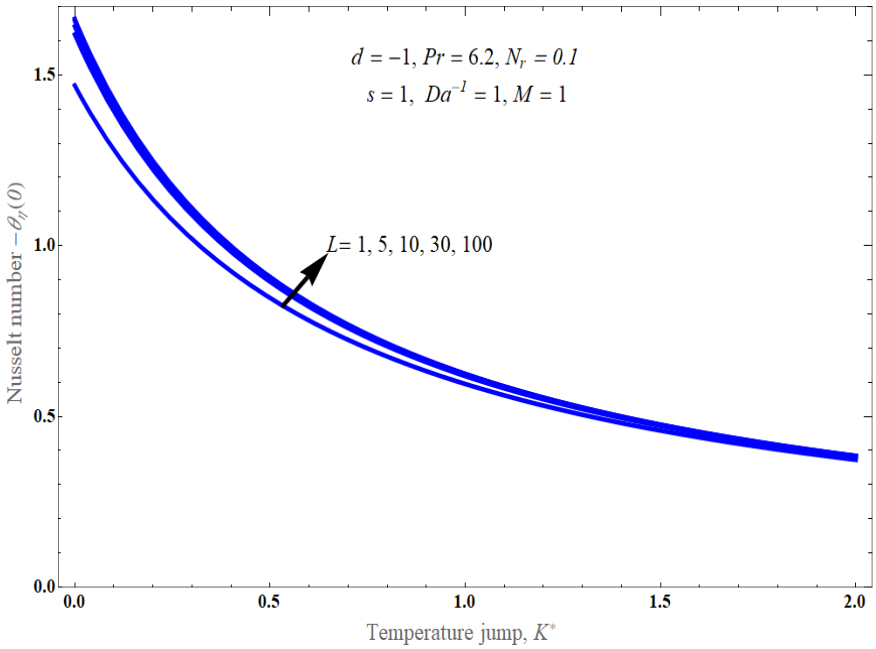


Figure 16. The impact of velocity slip on Nusselt number.

6. Conclusions

In this paper, analytical solutions were obtained for the laminar BL flow of Hnf past a porous stretching/shrinking sheet affected by mass suction/injection when radiation and MHD are present. The impacts of velocity slip condition, temperature increase, and inverse Darcy number were also analyzed. The dominating basic equations are approximated by a series of nonlinear ODEs using similarity conversion. The impacts of relevant factors on the velocity, temperature, skin friction, and Nusselt number profiles were explored. The subsequent list of primary results of the current research:

i. Because of the strong magnetic field, inverse Darcy number, and velocity slip parameter, the non-dimensional velocity profile reduces along the flow region, while temperature increases.
ii. As the coefficient of temperature increases, the temperature profile decreases.
iii. The increased radiation improves heat transfer when the thermal BL increases.
iv. A dual solution exists for shrinking cases only.
v. As velocity slip increases in magnitude, the skin friction profile diminishes, while the opposite effect occurs in the Nusselt number profile.

The limited scenario for this research was based on several previous investigations.

- $\lim_{\substack{Da^{-1} \to \infty, \\ q_r \to 0,}}$ {Results of work}→{Results of Turkyilmazoglu et al. [28]}.
- $\lim_{\substack{Da^{-1} \to \infty, \\ q_r \to 0,}}$ {Results of work}→{Results of Mohamed et al. [25]}.

Author Contributions: Conceptualization, U.S.M.; methodology, T.M.; validation, T.M., L.M.P. and G.M.S.; formal analysis, U.S.M.; investigation, T.M.; data curation, writing—original draft preparation, U.S.M. and L.M.P.; writing—review and editing, I.V.S.; visualization, T.M. and G.M.S.; supervision, U.S.M. and I.V.S. All authors have read and agreed to the published version of the manuscript.

Funding: The author L.M.P. acknowledges financial support ANID through convocatoria nacional Subvención a Instalación en la academia Convocatoria año 2021, grant SA77210040. The author T. Maranna would like to thank the financial assistance received from Karnataka Science and Technology Society (KSTePS) under the programme of Karnataka DST-Ph. D fellowship for Science and Engineering: DST/KSTePS/Ph.D.Fellowship/MP-07:2023-24.

Data Availability Statement: All data that support this study are included within the article.

Conflicts of Interest: The authors declare that they have no competing financial interests or personal relationships that could have appeared to influence the work reported in this paper.

Nomenclature

Symbols

A_1, A_2, A_3, A_4, A_5	Constants (-)
B_0	Magnetic flux (*Tesla*)
d	Stretching/shrinking parameter (-)
Da^{-1}	Inverse Darcy number (-)
K_a	Permeability (NA^{-1})
K^*	Temperature increase (K)
k^*	Mean absorption $\left(\mathrm{cm}^{-1}\right)$
l_1	First-order slip (-)
L	Velocity slip (-)
M	Magnetic field (-)
N_r	Radiation (-)
Pr	Prandtl number (-)
q_r	Radiative heat flux $\left(\mathrm{Wm}^{-2}\right)$
s	Mass suction/injection (-)
T	Fluid temperature (K)
T_w	Wall temperature (K)
T_∞	Far temperature (K)
(u, v)	Velocity components $(\mathrm{m/s})$
x	Horizontal axis (-)
y	Vertical axis (-)

Greek symbols	
ρ_{hnf}	Density (kg/m^3)
$(\rho C_p)_{hnf}$	Heat capacitance (JK^{-1}kg^{-1})
σ_{hnf}	Electrical conductivity (S/m)
κ_{hnf}	Thermal conductivity (Wm^{-1}K^{-1})
ν_{hnf}	Kinematic viscosity (m^{2}s^{-1})
η	Similarity variable (-)
χ	Similarity variable (-)
ξ_1, ξ_2	Constants (-)
σ^*	Stefan–Boltzmann constant (-)
Subscripts	
Nf	Nanofluid (-)
Hnf	Hybrid nanofluid (-)
Abbreviations	
MHD	Magnetohydrodynamic
ODEs	Ordinary differential equations
PDEs	Partial differential equations
BL	Boundary layer

References

1. Choi, S.U.S. Enhancing thermal conductivity of fluids with nanoparticles, Development and Applications of Non-Newtonian flows. *J. Heat Transf.* **1995**, *66*, 99–105.
2. Crane, L.J. Flow past a stretching plate. *Z. Angew. Math. Phys.* **1970**, *21*, 645–647. [CrossRef]
3. Hayat, T.; Nadeem, S. Heat transfer enhancement with Ag–CuO/water hybrid nanofluid. *Results Phys.* **2017**, *7*, 2317–2324. [CrossRef]
4. Sun, B.; Guo, Y.; Yang, D.; Li, H. The effect of constant magnetic field on convective heat transfer of Fe_3O_4/water magnetic nanofluid in horizontal circular tubes. *Appl. Term. Eng.* **2020**, *171*, 114920. [CrossRef]
5. Yarmand, H.; Gharehkhani, S.; Ahmadi, G.; Shirazi, S.F.S.; Baradaran, S.; Zubir, M.N.M.; Alehashem, M.S.; Dahari, M. Graphene nanoplatelets-silver hybrid nanofluids for enhanced heat transfer. *Energy Conv. Manag.* **2015**, *100*, 419–428. [CrossRef]
6. Waini, I.; Ishak, A.; Pop, I. Hybrid nanofluid flow and heat transfer past a permeable stretching/shrinking surface with a convective boundary condition. *J. Phys Conf. Ser.* **2019**, *1366*, 012022. [CrossRef]
7. Mahabaleshwar, U.S.; Anusha, T.; Hatami, M. The MHD Newtonian hybrid nanofluid flow and mass transfer analysis due to super-linear stretching sheet embedded in porous medium. *Sci. Rep.* **2021**, *11*, 22518. [CrossRef] [PubMed]
8. Sneha, K.N.; Mahabaleshwar, U.S.; Bhattacharyya, S. An effect of thermal radiation on inclined MHD flow in hybrid nanofluid over a stretching/shrinking sheet. *J. Therm. Anal. Calorim.* **2023**, *148*, 2961–2975. [CrossRef]
9. Zainal, N.A.; Nazar, R.; Naganthran, K.; Pop, I. Stability analysis of MHD hybrid nanofluid flow over a stretching/shrinking sheet with quadratic velocity. *Alex. Eng. J.* **2021**, *60*, 915–926. [CrossRef]
10. Devi, S.P.A.; Devi, S.S.U. Numerical investigation of hydromagnetic hybrid Cu—Al_2O_3/water nanofluid flow over a permeable stretching sheet with suction. *Int. J. Nonlinear Sci. Numer. Simul.* **2016**, *17*, 249–257. [CrossRef]
11. Tripathi, J.; Vasu, B.; Beg, O.A.; Gorla, R.S.R. Unsteady hybrid nanoparticle—Mediated magneto—Hemodynamics and heat transfer through an overlapped stenotic artery: Biomedical drug delivery simulation. *Proc. Inst. Mech. Eng. Part H* **2021**, *235*, 1175–1196. [CrossRef] [PubMed]
12. Asghar, A.; Ying, T.Y. Three dimensional MHD hybrid nanofluid flow with rotating stretching/shrinking sheet and joule heating. *CFD Lett.* **2021**, *13*, 1–19.
13. Mahabaleshwar, U.S.; Vishalakshi, A.B.; Anderson, H.I. Hybrid nanofluid flow past a stretching/shrinking sheet with thermal radiation and mass transpiration. *Chin. J. Phys.* **2022**, *75*, 152–168. [CrossRef]
14. Reddy, P.S.; Sreedevi, P.; Chamkha, A.J. Hybrid nanofluid heat and mass transfer characteristics over a stretching/shrinking sheet with slip effects. *J. Nanofluids* **2023**, *12*, 251–260. [CrossRef]
15. Tulu, A.; Ibrahim, W. Mixed convection hybrid nanofluids flow of MWCNTs-Al_2O_3/engine oil over a spinning cone with variable viscosity and thermal conductivity. *Heat Transf.* **2021**, *50*, 3776–3799. [CrossRef]
16. Rosca, N.C.; Rosca, A.V.; Aly, E.H.; Pop, I. Flow and heat transfer past a stretching/shrinking sheet using modified Buongiorno nanoliquid model. *Mathematics* **2021**, *9*, 3047. [CrossRef]
17. Bakar, S.A.; Arifin, N.M.; Bachok, N.; Ali, F.M. Effect of thermal radiation and MHD on hybrid Ag—TiO_2/H_2O nanofluid past a permeable porous medium with heat generation. *Case Stud. Therm. Eng.* **2021**, *28*, 101681. [CrossRef]
18. Gul, H.; Ramzan, M.; Chung, J.D.; Chu, Y.M.; Kadry, S. Multiple slips impact in the MHD hybrid nanofluid flow with Cattaneo-Christov heat flux and autocatalytic chemical reaction. *Sci. Rep.* **2021**, *11*, 14625. [CrossRef]

19. Jiang, X.; Hatami, M.; Abderrahmane, A.; Younis, O.; Makhdoum, M.B.; Guedri, K. Mixed convection heat transfer and entropy generation of MHD hybrid nanofluid in a cubic porous cavity with wavy wall and rotating cylinders. *Appl. Therm. Eng.* **2023**, *226*, 120302. [CrossRef]
20. Tulu, A. Numerical analysis of magnetohydrodynamic and dissipated hybrid casson nanofluid flow over an unsteady stretchable rotating disk with Cattaneo-Christov heat flux model. *J. Nanofluids* **2023**, *12*, 1748–1760. [CrossRef]
21. Tulu, A.; Ibrahim, W. Effects of second-order slip flow and variable viscosity on natural convection flow of (CNTs-Fe_3O_4)/water hybrid nanofluids due to stretching surface. *Math. Probl. Eng.* **2021**, *6*, 8407194.
22. Kumar, T.S. Hybrid nanofluid slip flow and heat transfer over a stretching surface. *Partial. Differ. Equ. Appl. Math.* **2021**, *4*, 100070. [CrossRef]
23. Das, K.; Acharya, N.; Tausif, S.K.M.; Duari, P.R.; Chakraborty, T. Slip flow of hybrid nanofluid in presence of solar radiation. *Int. J. Mod. Phys. C* **2022**, *33*, 2250017. [CrossRef]
24. Mohamed, M.K.A.; Ong, H.R.; Alkasasbeh, H.T.; Salleh, M.Z. Heat transfer of Ag-Al_2O_3/ water hybrid nanofluid on a stagnation point flow over a stretching sheet with Newtonian heating. *J. Phys. Conf. Ser.* **2020**, *1529*, 042085. [CrossRef]
25. Dinarvand, S.; Yousefi, M.; Chamkha, A.J. Numerical simulation of unsteady flow towards a stretching/shrinking sheet in a porous medium filled with hybrid nanofluid. *J. Appl. Comput. Mech.* **2022**, *8*, 11–20.
26. Prakash, O.; Rao, P.S.; Sharma, R.P.; Mishra, S.R. Hybrid nanofluid MHD motion towards an exponentially stretching/shrinking sheet with the effect of thermal radiation, heat source and viscous dissipation. *Pramana* **2023**, *64*, 97. [CrossRef]
27. Turkyilmazoglu, M. Exact analytical solutions for heat and mass transfer of MHD slip flow in nanofluids. *Chem. Eng. Sci.* **2021**, *84*, 182–187. [CrossRef]
28. Abel, M.S.; Shambajee, N.R.S. Effects of velocity and solutal slip boundary conditions on the flow and heat transfer of nanofluids past a linear stretching sheet with prescribed constant wall temperature. *Int. J. Emerg. Technol.* **2016**, *7*, 393–403.
29. Shobha, K.C.; Mallikarjun, B.P. Effect of non-linear thermal radiation on flow of Williamson nanofluid in a vertical porous channel with heat source or sink by using Adomian decomposition method. *J. Nanofluids* **2022**, *11*, 39–47. [CrossRef]
30. Mahabaleshwar, U.S.; Maranna, T.; Perez, L.M.; Bognar, G.V.; Oztop, H.F. An impact of radiation on laminar flow of dusty ternary nanofluid over porous stretching/shrinking sheet with mass transpiration. *Results Eng.* **2023**, *18*, 101227. [CrossRef]
31. Maranna, T.; Mahabaleshwar, U.S.; Ravichandra Nayakar, S.N.; Sarris, I.E.; Souayeh, B. An influence of radiation and magnetohydrodynamic flow of hybrid nanofluid past a stretching/shrinking sheet with mass transpiration. *ZAMM Z. Fur Angew. Math. Mech.* **2023**, *103*, e202300140. [CrossRef]
32. Suneetha, K.; Ibrahim, S.M.; Kumar, P.V.; Jyothsna, K. Linear thermal radiation effects on MHD viscoelastic fluid flow through porous moving plate with first order chemical reaction, variable temperature and concentration. *J. Comput. Appl. Res. Mech. Eng.* **2021**, *10*, 496–509.
33. Tulu, A.; Asefa, L.; Sohail, M. Unsteady magnetohydrodynamic hybrid nanofluid flow over a rotating disk with viscous dissipation and Cattaneo-Christov heat flux model. *Int. J. Thermofluids* **2024**, *21*, 100586. [CrossRef]
34. Khashi'ie, N.S.; Arifin, N.M.; Pop, I. Unsteady axisymmetric radiative Cu-Al_2O_3 flow over a radially stretching/shrinking surface. *Chin. J. Phys.* **2022**, *78*, 169–179. [CrossRef]
35. Zainodin, S.; Jamaludin, A.; Nazar, R.; Pop, I. MHD mixed convection of hybrid ferrofluid flow over an exponentially stretching/shrinking surface with heat source/sink and velocity slip. *Mathematics* **2022**, *10*, 4400. [CrossRef]

Disclaimer/Publisher's Note: The statements, opinions and data contained in all publications are solely those of the individual author(s) and contributor(s) and not of MDPI and/or the editor(s). MDPI and/or the editor(s) disclaim responsibility for any injury to people or property resulting from any ideas, methods, instructions or products referred to in the content.